Probing the local distortion of Fe sites in Fe 3 O 4 thin-films using enhanced symmetry selection in XMLD

Hebatalla Elnaggar, Rupan Wang, Mahnaz Ghiasi, Maria Yañez, Mario U Delgado-Jaime, Mai Hussein Hamed, Amelie Juhin, Sarnjeet S Dhesi, Frank de Groot

Probing the local distortion of Fe sites in Fe_3O_4 thin-films using enhanced symmetry selection in XMLD

Hebatalla Elnaggar,[1,*] RuPan Wang,[1] Mahnaz Ghiasi,[1] Maria Yañez,[2] Mario U. Delgado-Jaime,[2] Mai Hussein Hamed,[3,4] Amélie Juhin,[5] Sarnjeet S. Dhesi,[6] and Frank de Groot[1,†]

[1] *Debye Institute for Nanomaterials Science, 3584 CG Utrecht, The Netherlands*
[2] *University of Guadalajara, Blvd. Marcelino Garcia Barragan 1421, esq Calzada Olimpica, C.P. 44430, Guadalajara, Jalisco, Mexico*
[3] *Peter-Grünberg-Institut, Forschungszentrum Jülich GmbH, 52425 Jülich, Germany*
[4] *Faculty of Science, Helwan University, 11795 Cairo, Egypt*
[5] *Institut de Minéralogie, de Physique des Matériaux et de Cosmochimie, CNRS, Sorbonne Université, MNHN, UMR7590, 75252 Paris Cedex 05, France.*
[6] *Diamond Light Source, Harwell Science and Innovation Campus, Didcot OX11 0DE, UK*

Magnetite (Fe_3O_4) thin-films are among the most stimulating systems for electronic applications, in particular given that their electric and magnetic properties can be controlled by substrate strain. Here we investigate the electronic structure of a 38 nm $Fe_3O_4/SrTiO_3$ (001) thin-film by a unique set of X-ray magnetic linear dichroism (XMLD) measurements. We show that it is only possible to uncover the orbital character of the Fe sites in Fe_3O_4 by a systematic analysis of the XMLD angular distribution. The local symmetry of the Fe^{2+} B site in the thin-film is found to be trigonally distorted. Our results highlight that the combination of state-of-the-art XMLD measurements and theoretical simulations is indispensable for investigating the electronic structure of oxide thin-films and heterostructures.

I. INTRODUCTION

Oxide heterostructures provide a fruitful playground to generate tuneable properties that can be engineered for electronic, spintronic, multiferroic and magnetic devices[1–5]. One of the most intriguing oxide systems is magnetite (Fe_3O_4), which in the form of thin-films, is ideal for spintronic applications because of its half metallicity and strong spin polarization at the Fermi level[6–8]. Moreover, Fe_3O_4 exhibits a metal to insulator transition, the Verwey transition, at T_V ∼125K which results in a spontaneous change of both the lattice symmetry and the electric conductivity[9,10]. Verwey proposed that at T_V a charge ordering transition takes place[10] which gave rise to considerable efforts devoted to finding evidence for the proposed charge ordering[11–14]. This drastic change in conductivity was also found to occur on the picosecond timescale[15,16] opening novel avenues for designing fast electronics.

Above T_V, Fe_3O_4 has a cubic inverse spinel crystal structure (space group $Fd\bar{3}m$, a_{Bulk} = 8.3965 Å[17]) containing two different Fe sites. Figure 1 illustrates how the Fe_3O_4 inverse spinel crystal structure consists of Fe^{3+} ions in tetrahedral coordination (A sites), and Fe^{2+} and Fe^{3+} ions (or, on average, $Fe^{2.5+}$) in nearly octahedral coordination (B sites formally belonging to the $\bar{3}m$ point group) with O^{2-} ions in a FCC lattice[17]. The Fe A and B sublattices are antiferromagnetically coupled while the Fe ions at the B sublattice are ferromagnetically coupled (Figure 1) leading to a Curie temperature of T_C ∼ 860 K.

High quality single crystal thin-films of Fe_3O_4 can be epitaxially grown, interfaced and integrated on different substrates such as MgO (a = 4.212 Å), $SrTiO_3$ (a = 3.905 Å) and $MgAl_2O_4$ (a = 8.0831 Å)[18–23] providing an appropriate architecture for technological device integration. The resulting electronic and magnetic properties of the thin-films are governed by growth characteristics such as strain, stoichiometry and defect states[20–26]. It is in fact a highly non-trivial task to predict the resulting properties given the closely competing energy scales (such as distortion, exchange, Kugel-Khomskii and spin-orbit coupling) which cause the properties to be strongly dependent on small changes in the atomic structure. For example, recent studies showed that it is possible to modify the Verwey transition temperature of Fe_3O_4 by tuning the lattice mismatch by 0.66%[20,26].

Although the use of strain energy imposed by epitaxial growth is one of the primary routes to engineering

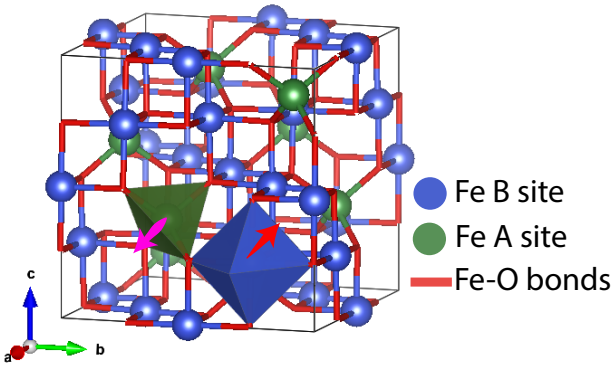

FIG. 1. Schematics of the inverse spinel Fe_3O_4 cubic unit cell, where Fe^{3+} cations (green) occupy tetrahedral A sites while both Fe^{2+} and Fe^{3+} cations (blue) occupy nearly octahedral B sites. The B (red arrow) and A sites (magenta arrow) are antiferromagnetically coupled.

the properties of Fe_3O_4 thin-films, its effect on the electronic structure remains controversial. As the Verwey transition is associated with charge and orbital ordering, being able to control it with strain requires a detailed microscopic understanding of the local Fe electronic and magnetic structure. It is therefore desirable to sensitively probe the charge, spin, and orbital degrees of freedom of the Fe ions in Fe_3O_4 to determine the effect of strain on the local site symmetry. This remains a task beyond standard techniques such as diffraction and scanning transmission electron microscopy (STEM) because the oxygen positions are not easily determined.

In this work, we use XMLD measurements at the Fe $L_{2,3}$-edge of Fe_3O_4 (38 nm, a_{Film} = 8.36 Å as detailed in Figure S2) grown on an $SrTiO_3$ (001) substrate to study the electronic and magnetic structure of the Fe sites in the thin-film. The large lattice mismatch between $SrTiO_3$ and Fe_3O_4 ($\sim$ 7.5%[27]) makes it an interesting heterostructure to investigate, in particular, given that $SrTiO_3$ is a backbone electrode material for oxide electronics. The thickness of the film lies in between the critical thickness, t_{crit} = 7 nm and $10t_{crit}$ where structural relaxation and reconstructions are predicted to occur[21,24]. Such distortion can have dramatic effects by modifying orbital degeneracies, and in turn orbital ordering patterns.

We demonstrate here that it is possible to unambiguously determine the symmetry of Fe ions in Fe_3O_4 through a systematic analysis of the angular dependent XMLD signal. Furthermore, we show that the small Jahn-Teller distortions can be best determined when the XMLD signal is measured in an optimized configuration. Our measurements combined with theoretical simulations reveal that the nominal Fe^{2+} B sites of the $Fe_3O_4/SrTiO_3$ thin-film are trigonally distorted. The distortion parameter concluded is consistent in sign and close in magnitude to that of bulk Fe_3O_4. The methodology developed here provides a blueprint for the characterization of thin-films where the interplay between various interactions, such as magnetic exchange, spin-orbit coupling and the Jahn-Teller distortion, all play a role in determining the low energy state.

II. METHODOLOGY

A. Experimental details

The Fe_3O_4 thin-film was grown on a conductive 0.1% Nb-doped $SrTiO_3$ (001) TiO_2-terminated substrate by pulsed laser deposition (PLD) as described by Hamed *et. al.*[19]. Briefly, the substrate temperature and oxygen partial pressure were kept at 400 °C and 2×10^{-6} mbar, respectively. We used a laser fluence of 1.5 J/cm^2 with a repetition rate of 5 Hz producing ionized particles from a Fe_2O_3 (purity 99.9%) rotating target. In this setup, the substrate was mounted 50 mm away from the target.

The film thickness, interface and surface roughness were examined by X-ray reflectivity (XRR) with Cu K_α-radiation as shown in Figure S1. The epitaxial growth condition was checked using XRD measurements reported in Figure S2. Bulk magnetic properties were investigated by a vibrating sample magnetometer using a quantum design dynacool physical properties measurement system. The magnetic moment versus temperature, M(T), was measured in zero field cooling (ZFC) mode with 500Oe applied field to determine the Verwey transition as shown in Figure S3. Hysteresis loops were recorded with a magnetic field, $B = \pm 5$ T, applied parallel to the in-plane [100] direction (see Figure S4).

X-ray magnetic circular dichroism (XMCD) and XMLD measurements were carried out on beamline I06 of Diamond Light Source, U.K. The beam spot at the sample position is estimated to be $\sim 200\,\mu\text{m} \times 100\,\mu\text{m}$. A vector magnet set to $B = 1$ T was used to saturate the magnetization to any arbitrary direction. All measurements were performed at $T = 200$ K in a normal incidence configuration, *i.e.* with the incoming beam impinging at an angle of 90° with respect to the sample surface. The energy resolution is estimated to be $\sim$ 200 meV full width half maximum (FWHM). The measurements were performed in total electron yield (TEY) and fluorescence yield (FY) mode.

All experimental spectra were first normalized to the incident photon flux. The spectra were then fitted using a model consisting of two error functions to take into account the $L_{2,3}$ edge jumps. In addition, a set of Gaussian functions were used to fit the multiplet features of the spectra (refer to the SupplementaryInformation for more details). The $L_{2,3}$ edge jumps were subtracted from the spectra and the spectra were renormalized to the spectral area.

B. Theoretical simulations

Crystal field multiplet calculations were performed using the quantum many-body program Quanty[28–30]. Three independent Fe sites were considered for the calculations, namely, Fe^{2+} in octahedral symmetry (O_h), Fe^{3+} in octahedral symmetry (O_h), and Fe^{3+} in tetrahedral symmetry (T_d). The Hamiltonian used for the calculations involved the following terms: (i) Coulomb interaction, (ii) crystal field potential, (iii) spin-orbit coupling and (iv) magnetic exchange interaction as detailed in[31]. The optimized parameters used for the calculations are reported in Table S4, Table S5 and Table S6 of the supplementary information. Two sets of calculations were performed:

1. Calculations for strained Fe_3O_4 thin-film where the effects of substrate bi-axial induced distortion were simulated by reducing the nominal point group symmetry of Fe^{2+} ions to tetragonal symmetry (D_{4h}).

2. Calculations for a relaxed Fe_3O_4 thin-film where

four trigonally distorted (D_{3d}) $Fe^{2+}O_6$ clusters were taken into consideration to simulate bulk-like Fe_3O_4 (see supplementary information for more details).

The choice of the magnitude of the distortion parameters were based on the effect on the XMLD features (see Figure S10 and Figure S11 for more details). We note that we investigated the effect of distortion only at the nominal Fe^{2+} ion because the $^5D_4$ ground state of the Fe^{2+} ion is strongly influenced by distortion while the $^6A_1$ ground state of the Fe^{3+} ions does not split by distortion to a first approximation. A comparison between calculations of the Fe^{3+} XMLD spectra with and without distortion are presented in Figure S7 and Figure S8.

III. RESULTS

A. Limitations of XMCD in mixed valence systems

Soft X-ray absorption spectroscopy (XAS) and XMCD techniques have developed into powerful tools to characterize magnetic thin-films[32]. XAS can be used to determine the electronic state of the transition metal[33] while sum rules applied to the XMCD allows the spin and orbital magnetic moments to be determined[34,35]. However, the lifetime broadening of the XAS spectra at $L_{2,3}$-edges (~ 0.2 eV) imposes a challenge to the identification and quantification of small distortions induced in thin-films, particularly given the rich multiplet states[36]. This limitation is even more pronounced for mixed valence systems, such as Fe_3O_4, where the XAS spectra are broader because multiple ions contribute to the signal. Only four peaks can be clearly identified from the L_3 XAS measurements at ~ 706 eV, 707.5 eV, 709 eV and and 710 eV as shown by the vertical ticks in Figure 2a.

The experimental XMCD signal of Fe_3O_4 is shown in Figure 2a. The spectral shape is consistent with previously reported measurements[37–41]. A detailed comparison between XMCD measurements of the thin-film and bulk Fe_3O_4 is presented in Figure S9. Three main peaks are observed at the L_3 region of the XMCD indicated by the vertical ticks, namely at 707.5 eV, 709 eV, and 710 eV. The first and the third peak have the same sign (positive dichroism) while the second peak exhibits an opposite dichroism. The three peaks are associated mainly with the Fe^{2+} B ions (707.5 eV), Fe^{3+} A ions (709 eV), and Fe^{3+} B ions (710 eV) as shown in Figure 2e. For this reason, the ferromagnetically coupled Fe B ions have the same sign of XMCD while the antiferromagnetically coupled Fe A ions have an opposite XMCD sign.

In order to investigate the effect of local distortions on XMCD spectra we computed the theoretical XMCD spectra considering perfectly octahedral (O_h), tetragonal (D_{4h}) and trigonal (D_{3d}) distorted ions at the Fe^{2+} B sites. Despite some minor differences between the three simulations (compare the calculations presented in Figure 2b, c and d), it is not possible to unambiguously determine the local symmetry of the Fe ions from the XMCD signal. This uncertainty regarding the local symmetry obscures the quantification of the ion percentages which is commonly determined using XMCD[42]. We found a nearly 4% difference in the quantification between the three simulations (See Table S7). Moreover, the orbital moments deduced from these simulations using the three local symmetries are significantly different as shown in Table I. This ambiguity then strongly limits the information that can be deduced from such measurements on complex systems.

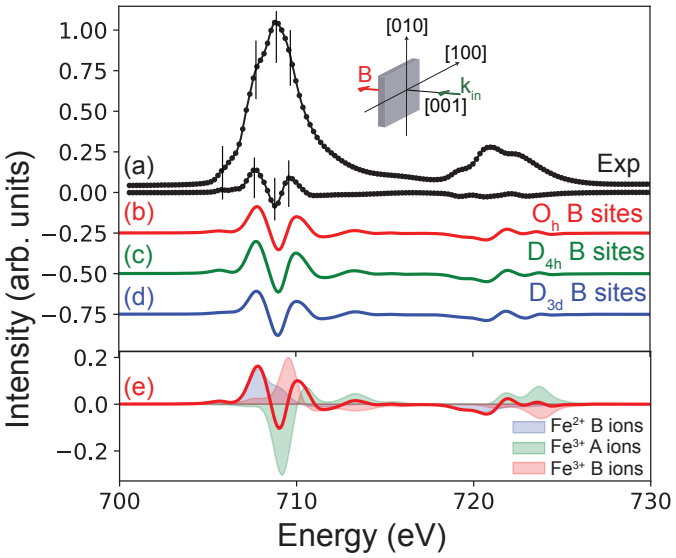

FIG. 2. Fe $L_{2,3}$ XAS and XMCD spectra from Fe_3O_4 measured in TEY mode. (a) Experimental XAS and XMCD spectra of a Fe_3O_4 thin-film. The positions of the main peaks observed for XAS and XMCD are shown by the vertical ticks. Multiplet calculations of the XMCD signal are shown in (b), (c) and (d) for three distortion types at the Fe^{2+} B sites, namely, octahedral (O_h), tetragonal ($D_{4h}, D_s = 0.1eV$), and trigonal ($D_{3d}, D_\sigma = 0.1eV$). The individual contributions of the Fe ions to the XMCD signal is shown in (e). A sketch of the experimental geometry is shown at the top of the figure.

Symmetry	**Magnetic moment** (μ_B)	
	Spin	Orbital
O_h	-3.9425 ±0.0002	-0.98 ±0.03
D_{4h}, $D_s = 0.1$ eV	-3.958 ±0.007	-0.25 ±0.05
D_{3d}, $D_\sigma = 0.1$ eV	-3.983 ±0.004	-0.22 ±0.02

TABLE I. Computed magnetic spin and orbital moments of Fe^{2+} B sites in three local symmetries, namely, octahedral (O_h), tetragonal (D_{4h}), and trigonal (D_{3d}). The reported errors are obtained from the errors in the distortion parameters $10D_q$, D_s and D_σ respectively.

B. X-ray magnetic linear dichroism

XMLD has recently gained attention in studying the magnetic properties of thin-films and especially for antiferromagnetic systems[43–51]. XMLD can be obtained by the difference in the XAS cross-section measured with linearly polarized light and two perpendicular orientations of the magnetic field or fixed orientation of the field and two perpendicular light polarizations. Details of the possible configurations that can be used to measure XMLD was discussed by Arenholz *et. al.*[49]. It can be used to determine the anisotropic magnetic moments and the anisotropic spin-orbit interaction[52–55]. Such information is valuable for understanding and harnessing the magnetic properties of thin-films and multilayers. However, the analysis of XMLD is far from being straightforward because the signal includes structural (crystal field) and magnetic effects. This implies that XMLD is strongly affected by the relative orientation of the external magnetic field ($\boldsymbol{B}$), X-ray polarization ($\boldsymbol{\epsilon}$), and the crystalline axes. A systematic XMLD measurement combined with theoretical simulations can shed light on the origin of the signal and reveal many fine details of the electronic and the magnetic structure. We measured the XMLD signal with linear horizontal polarized X-rays (LH, *i.e.* $\epsilon \parallel [100]$) with the external field parallel to the [100] ($\phi = 0°$) and parallel to [010] ($\phi = 90°$) as described in Figure 3a. The experimental XMLD signal exhibits a more complex structure in comparison to the XMCD (Compare Figure 3c to Figure 2a). Theoretical simulation of the XMLD for perfectly octahedral Fe B sites is shown in Figure 3d. The simulation misses two features at 719 eV and 722.5 eV indicated by the red arrows in the figure. We measured the XMLD angular dependence from $\phi = 0°$ to $\phi = 90°$ to ensure that the difference between the experimental data and the simulation is not due to a slight misalignment of the sample. The two features at 719 eV and 722.5 eV are missing for the full angular range as can be seen in Figure 3e and f.

The discrepancy between the experiment and simulations is linked to the assumption made regarding the local symmetry of the Fe ions. On one hand, the lattice mismatch between the $SrTiO_3$ substrate and Fe_3O_4 can distort the local symmetry. In this case, an in-plane tetragonal compressive distortion would be expected. On the other hand, the point group symmetry of the Fe B sites of bulk Fe_3O_4 is trigonal and hence if the film is relaxed, a trigonal distortion is expected. We investigated the two possible scenarios by simulating the XMLD expected for tetragonally and trigonally distorted Fe B sites. The theoretical XMLD angular dependence computed for tetragonal and trigonal distortions are presented in Figure 4. Simulations using the distortion parameters $D_s = 0.1$ eV (Figure 4a) and $D_\sigma = 0.1$ eV (Figure 4c) now reproduce the features at 719 eV and 722.5 eV. Our simulations thus confirm that in plane compressive tetragonal distortion and trigonal bulk Fe_3O_4 like-distortion are both compatible with the observed dichroism signal. On the other hand, calculations with $D_s = -0.1$ eV (Figure 4b) and $D_\sigma = -0.1$ eV (Figure 4d) are incompatible.

C. Optimized XMLD angular dependence

Next, we measured the XMLD angular dependence with the incident polarization rotated 30° with respect to the [100] orientation (see Figure 5a). This orientation does not coincide with a high symmetry axis and hence is expected to provide insights into the nature of the local distortions. The experimental angular dependence is shown in Figure 5b. Although the simulations done with tetragonal ($D_s = 0.1$ eV, Figure 5c) and trigonal ($D_\sigma = 0.1$ eV, Figure 5d) distortion both reproduce the general spectral shape, the ratio between the features at 707 eV and 708 eV is only captured by the trigonal symmetry (black arrows in Figure 5b). The sign and the magnitude of the distortion is consistent with that of bulk Fe_3O_4 ($D_{\sigma,bulk} = 0.07$ eV). This means that the film has nearly fully relaxed at a thickness of only $\sim 6t_{crit}$.

Comparison between the XMLD measured with TEY and FY could provide insights into the surface versus "bulk" properties of the thin-film. Experiments detected in TEY are surface sensitive because the electron escape range is limited to few nanometers (~ 4.5 nm in Fe_3O_4 as reported by Gota *et. al.*[56]). On the other hand, the penetration depth of soft X-rays are in the order of tens of nanometers[57], *i.e.* comparable to the full thickness of the thin-film. This however also means that the FY signal is largely affected by saturation and self absorption effects and the spectral shape is consequently modified. We compared the FY results to fully strained and fully relaxed theoretical simulations in Figure S13 of the supplementary information. Although the tetragonal distortion ($D_s = 0.1$ eV) shows better agreement with the experimental XMLD, it can not reproduce all aspects of the spectra. This is likely due to the formation of multi-domains composed of stressed and relaxed regions. It is difficult to quantify these domains from the current set of data because of the uncertainties imposed by the self-absorption and saturation effects. A systematic measurement of the XMLD angular dependence as a function of the film thickness could be used to quantify these domains and determine the experimental critical thickness at which these domains start to form in future experiments.

D. Origin of the symmetry selectivity

It is of theoretical and practical interest to understand the origin of the symmetry selectivity obtained for the measurements performed with the polarization aligned 30° from the [100] axis. This serves as a guide to design efficient experiments that can distinguish the local site symmetry and quantify the distortion parameters. A close inspection of the dependence of the XAS pro-

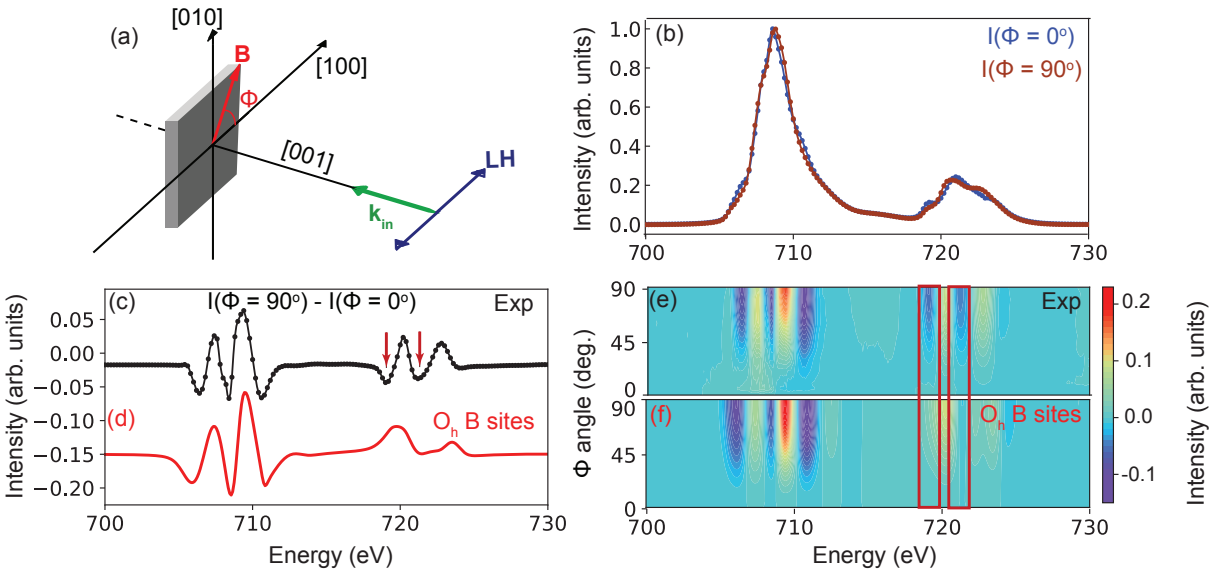

FIG. 3. Fe $L_{2,3}$ XMLD spectra from Fe_3O_4 detected in TEY mode. (a) A schematic of the experimental geometry. The linear horizontal polarization (LH) is aligned parallel to [100]. The XMLD signal is computed by subtracting the XAS signal measured with the external magnetic field (**B**) parallel to [100] ($\phi = 0°$) from that measured with **B** parallel to [010] ($\phi = 90°$). $\mathbf{k_{in}}$ is the incident wave vector. (b) XAS measurements $I(\phi = 0^o)$ and $I(\phi = 90^o)$. The experimental and theoretical XMLD signal are shown in (c) and (d). The experimental and theoretical XMLD angular dependence over 90° computed as $I(\phi) - I(\phi = 0°)$ are presented in panels (e) and (f) respectively.

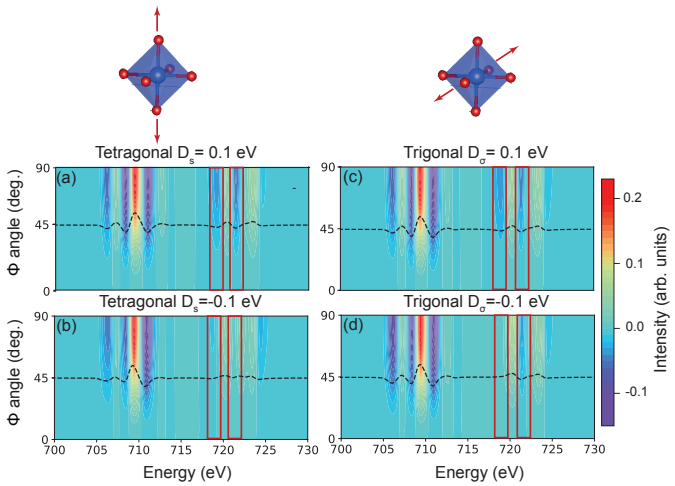

FIG. 4. Theoretical XMLD angular dependence over 90° computed as $I(\phi) - I(\phi = 0)$ for tetragonal symmetry (D_{4h}) with (a) $D_s = 0.1\,\text{eV}$, (b) $D_s = -0.1\,\text{eV}$. Calculations for trigonal symmetry (D_{3d}) with $D_\sigma = 0.1\,\text{eV}$ and $D_\sigma = -0.1\,\text{eV}$ are shown in panels (c) and (d). The XMLD at $\phi = 45°$ is shown as dashed lines.

cess on the polarization and the external magnetic field is therefore required. The general XAS cross-section can be expressed as in Equation (1) where ϵ is the polarization vector, ω is the frequency of the light, α is the fine structure factor, **Im** is the imaginary part of the equation and σ is the conductivity tensor[58] describing the materials properties[59].

$$XAS^{Dipole}(\boldsymbol{\epsilon}) = -4\pi\alpha\hbar\omega\mathbf{Im}\left[\boldsymbol{\epsilon}^* \cdot \sigma \cdot \boldsymbol{\epsilon}\right] \tag{1}$$

The conductivity tensor is a 3×3 matrix for a dipole transition as shown in Equation (2). The matrix elements of the conductivity tensor are defined in Equation (3) where ψ_i is the ground state wavefunction, $T_{x(y)} = \epsilon_{x(y)} \cdot r_{x(y)}$ is the dipole transition operator, H is the Hamiltonian of the final state and Γ is the lifetime broadening.

$$\sigma = \begin{bmatrix} \sigma_{xx} & \sigma_{xy} & \sigma_{xz} \\ \sigma_{yx} & \sigma_{yy} & \sigma_{yz} \\ \sigma_{zx} & \sigma_{zy} & \sigma_{zz} \end{bmatrix} \tag{2}$$

$$\sigma_{xy} = < \psi_i | T_y^\dagger \frac{1}{\omega - H + i\Gamma/2} T_x | \psi_i > \tag{3}$$

In the most general case, nine independent measurements are required to fully reconstruct the conductivity tensor. However, the crystal symmetry can simplify the conductivity tensor by dictating equivalence between matrix elements or canceling out some of the matrix elements. The conductivity tensor of an octahedral Fe^{2+} ion with the magnetic field aligned parallel to the high symmetry [100] axis (*i.e.* the x axis with ϕ =0°) is shown

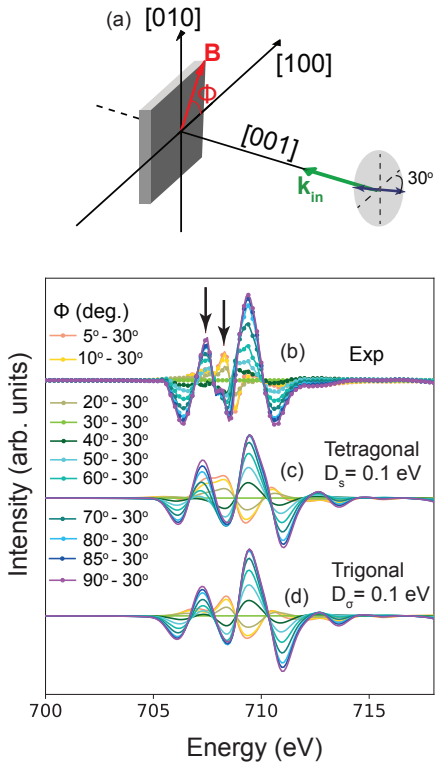

FIG. 5. Fe L_3 XMLD angular dependence in Fe_3O_4 measured in TEY mode. (a) A schematic of the experimental geometry. The polarization is aligned 30° from the [100] axis. The XMLD is computed as: $XAS[\phi] - XAS[\phi = 30°]$. (b) Experimental XMLD angular dependence. Theoretical simulations for tetragonal ($D_s = 0.1\,\text{eV}$) and trigonal ($D_\sigma = 0.1\,\text{eV}$) distortions are shown in (c) and (d) respectively.

in Figure 6a. Here, five of the nine matrix elements are finite (three diagonal elements: $\sigma_{xx}, \sigma_{yy}, \sigma_{zz}$ and two off-diagonal elements: σ_{yz} and σ_{zy}). The cubic crystal field implies that the x, y and z directions are equivalent by symmetry, however the magnetic field aligned to the x axis breaks the equivalency. For this reason, σ_{xx} is different from σ_{yy} and σ_{zz}. In addition, the x magnetic field induces off-diagonal terms σ_{yz} (σ_{zy}) leading to a scenario where an electric field in the z (y) direction can produce an excitation in the y (z) direction. Similarly, when the magnetic field is aligned along the [010] (y) axis (i.e. ϕ =90°), σ_{yy} becomes inequivalent to σ_{xx} and σ_{zz} and it induces $x - z$ off-diagonal terms (see Figure 6b).

An analogous behaviour is observed for tetragonal (Figure 6c and d) and trigonal (Figure 6e and f) calculations. Nonetheless, for the tetragonal case, the z axis is crystallographically inequivalent to the x and y axes. This is because the z direction is elongated with respect to the x and y due to the bi-axial in plane compression. We recall that the trigonal calculation comprises of a summation over four sites such that the cubic symmetry is preserved. For this reason, the trigonal calculations behave fully like the octahedral.

Aligning the polarization parallel to the [100] direction results in spectra that are only sensitive to the σ_{xx} matrix element. A comparison of the imaginary part of σ_{xx} at ϕ =0° for the three symmetries is shown in Figure 7. One concludes that the spectra are rather similar with the exception of the L_2 edge for the octahedral symmetry (Figure 7a). It is hence now clear why such a measurement is not optimum for the discrimination between the tetragonal and trigonal distortion. On the other hand, when the incident polarization is aligned 30° from the [100], it gains sensitivity to the σ_{xy}, σ_{yx} and σ_{yy} terms. These components are non-zero and significantly different between the three crystal systems when the magnetic field is also aligned to a low symmetry direction as shown for the off-diagonal element σ_{xy} in Figure 8. We therefore conclude that the reason for the symmetry selectivity achieved is due to:

1. The presence of off-diagonal matrix elements that are significantly different for the three crystal systems. These off-diagonal elements are induced by aligning the magnetic field to a low symmetry orientation (with respect to the crystal field).

2. Aligning the polarization such that it becomes sensitive to these inequivalent elements.

IV. CONCLUSION

We have observed strong XMLD in a Fe_3O_4 38 nm thin-film grown on 0.1% Nb-doped on a $SrTiO_3$ (001) TiO_2-terminated substrate. Based on the a high symmetry XMLD experimental geometry, it was concluded that the local symmetry of the Fe B sites of Fe_3O_4 are not perfectly octahedral. However, it was not possible to determine unambiguously the nature of the distortion. We demonstrated that it is possible to pinpoint the local symmetry of the Fe^{2+} ions in Fe_3O_4 by a systematic analysis of the XMLD signal in an optimized geometry. We found that the local symmetry of the Fe^{2+} B sites is trigonal with a distortion parameter D_σ =0.1 eV which is very close to that of bulk Fe_3O_4[60]. This implies that the top $\sim$ 5 nm thin-film are fully relaxed at this thickness. We have provided a detailed analysis of the XMLD signal and a guide to optimize the symmetry selectivity of an XMLD experiment. The methodology developed here has far-reaching implications especially for the investigation of the electronic structure of strain engineered oxide thin-films and heterostructures.

V. ACKNOWLEDGEMENTS

The synchrotron experiments were performed at the I06 beamline of Diamond Light Source, U.K under proposal number SI-17588. We are grateful for the help

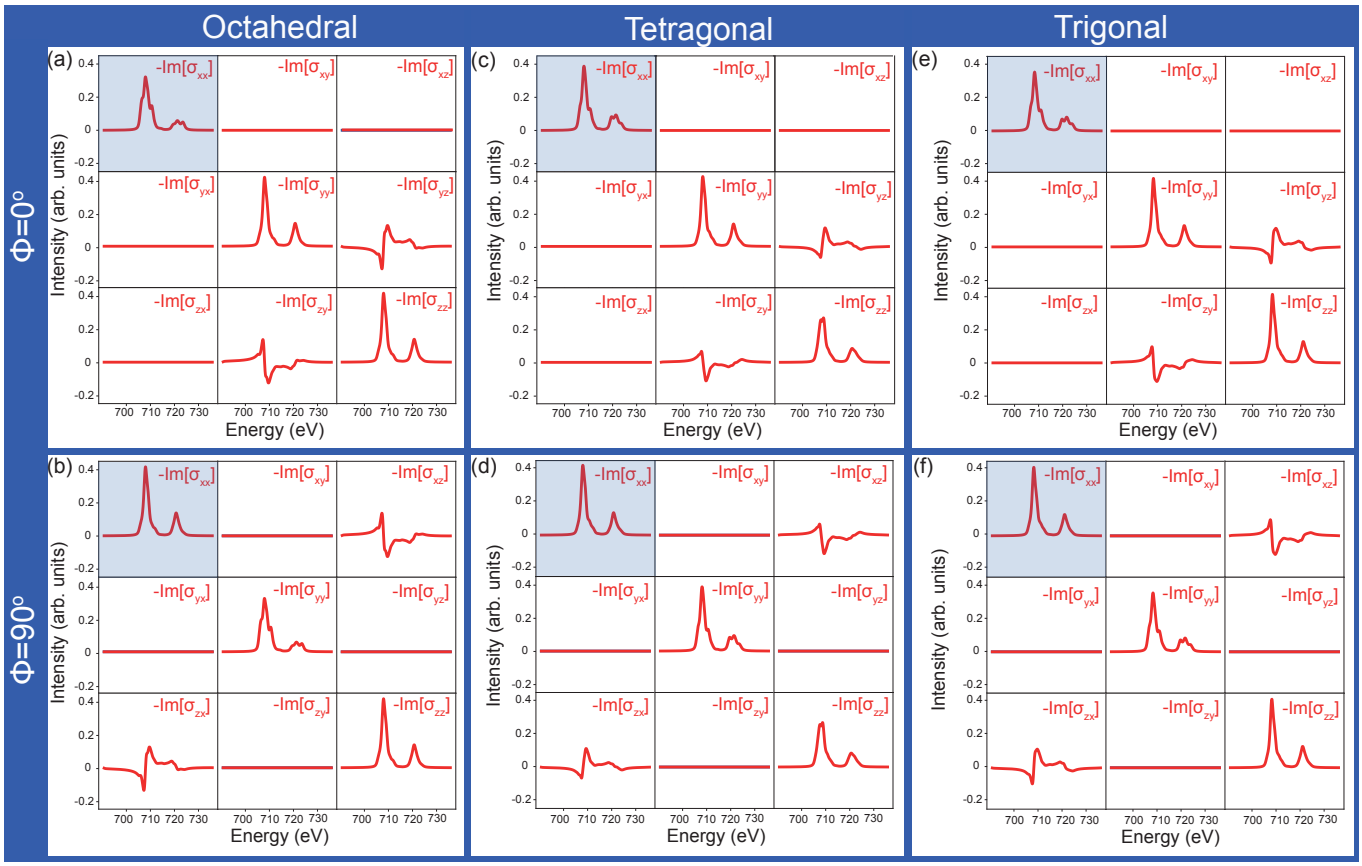

FIG. 6. $L_{2,3}$ Fe^{2+} conductivity tensor (σ) for the three studied crystal systems namely; octahedral, tetragonal ($D_s = 0.1\,\text{eV}$) and trigonal ($D_\sigma = 0.1\,\text{eV}$). The simulations in the first row are for $\phi = 0°$ (*i.e.* $\mathbf{B} \parallel [100]$) while the second row presents simulations done with $\phi = 90°$ (*i.e.* $\mathbf{B} \parallel [010]$).

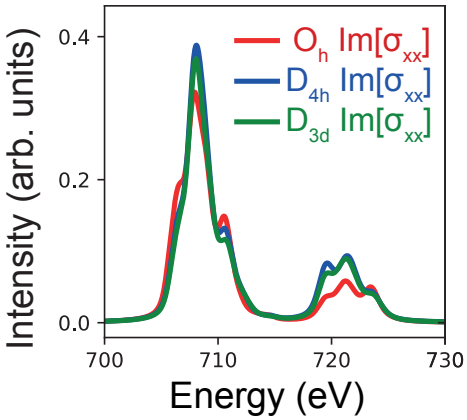

FIG. 7. The imaginary contribution of the Fe^{2+} $L_{2,3}$ diagonal matrix elements of the conductivity tensor (σ_{xx}) at $\phi = 0°$ for octahedral (red), tetragonal ($D_s = 0.1\,\text{eV}$ in blue), and trigonal ($D_\sigma = 0.1\,\text{eV}$ in green) distortion.

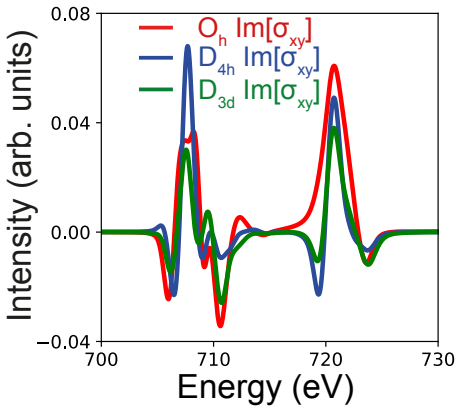

FIG. 8. The imaginary contribution of the $L_{2,3}$ Fe^{2+} off-diagonal element σ_{xy} at $\phi = 30°$ for octahedral (red), tetragonal ($D_s = 0.1\,\text{eV}$ in blue), and trigonal ($D_\sigma = 0.1\,\text{eV}$ in green) distortions.

of beamline I06 staff to setup and perform the experiments. We are thankful for the fruitful discussions with Ch. Brouder, P. Sainctavit, M.-A. Arrio and M. W. Haverkort. This work was financed by the ERC advanced Grant XRAYonACTIVE No. 340279.

* H.M.E.A.Elnaggar@uu.nl
† F.M.F.degroot@uu.nl

[1] J. van den Brink and D. I. Khomskii, J. Phys. Condens. Matter **20**, 434217 (2008).
[2] J.-B. Moussy, J. Phys. D Appl. Phys. **46**, 27 (2013).
[3] J. Ngai, F. Walker, and C. Ahn, Annu. Rev. of Mater. Res. **44**, 1 (2014).
[4] S. Dong, J.-M. Liu, S.-W. Cheong, and Z. Ren, Adv. Phys. **64**, 519 (2015).
[5] M. Huijben, G. Koster, Z. L. Liao, and G. Rijnders, Appl. Phys. Rev. **4**, 041103 (2017).
[6] A. Yanase and K. Siratori, J. Phys. Soc. Jpn **53**, 312 (1984).
[7] Z. Zhang and S. Satpathy, Phys. Rev. B **44**, 13319 (1991).
[8] V. N. Antonov, B. N. Harmon, and A. N. Yaresko, Phys. Rev. B **67**, 024417 (2003).
[9] E. J. W. Verwey, Nature **144**, 327 (1939).
[10] E. J. W. Verwey and P. W. Haayman, Physica **8**, 979 (1941).
[11] F. Walz, J. Phys. Condens. Matter **14**, R258 (2002).
[12] J. García and G. Subías, J. Phys. Condens. Matter **16**, R145 (2004).
[13] M. S. Senn, J. P. Wright, and J. P. Attfield, Nature **481**, 173 (2012).
[14] M. S. Senn, J. P. Wright, and J. P. Attfield, J. Korean Phys. Soc. **62**, 1372 (2013).
[15] N. Pontius, T. Kachel, C. Schüßler-Langeheine, W. F. Schlotter, M. Beye, F. Sorgenfrei, C. F. Chang, A. Föhlisch, W. Wurth, P. Metcalf, I. Leonov, A. Yaresko, N. Stojanovic, M. Berglund, N. Guerassimova, S. Düsterer, H. Redlin, and H. A. Dürr, Appl. Phys. Lett. **98**, 182504 (2011).
[16] S. de Jong, R. Kukreja, C. Trabant, N. Pontius, C. F. Chang, T. Kachel, M. Beye, F. Sorgenfrei, C. H. Back, B. Bräuer, W. F. Schlotter, J. J. Turner, O. Krupin, M. Doehler, D. Zhu, M. A. Hossain, A. O. Scherz, D. Fausti, F. Novelli, M. Esposito, W. S. Lee, Y. D. Chuang, D. H. Lu, R. G. Moore, M. Yi, M. Trigo, P. Kirchmann, L. Pathey, M. S. Golden, M. Buchholz, P. Metcalf, F. Parmigiani, W. Wurth, A. Föhlisch, C. Schüßler-Langeheine, and H. A. Dürr, Nat. Mater **12**, 882 EP (2013).
[17] C. Haavik, S. Stølen, H. Fjellvåg, M. Hanfland, and D. Häusermann, Am. Mineral. **85**, 514 (2000).
[18] M. Monti, M. Sanz, M. Oujja, E. Rebollar, M. Castillejo, F. J. Pedrosa, A. Bollero, J. Camarero, J. L. F. Cuñado, N. M. Nemes, F. J. Mompean, M. Garcia-Hernández, S. Nie, K. F. McCarty, A. T. N'Diaye, G. Chen, A. K. Schmid, J. F. Marco, and J. de la Figuera, J. Appl. Phys **114**, 223902 (2013).
[19] M. H. Hamed, R. A. Hinz, P. Lömker, M. Wilhelm, A. Gloskovskii, P. Bencok, C. Schmitz-Antoniak, H. Elnaggar, C. M. Schneider, and M. Müller, ACS Appl. Mater. Interfaces **11**, 7576 (2019).
[20] X. H. Liu, A. D. Rata, C. F. Chang, A. C. Komarek, and L. H. Tjeng, Phys. Rev. B **90**, 125142 (2014).
[21] S. Kale, S. M. Bhagat, S. E. Lofland, T. Scabarozi, S. B. Ogale, A. Orozco, S. R. Shinde, T. Venkatesan, B. Hannoyer, B. Mercey, and W. Prellier, Phys. Rev. B **64**, 205413 (2001).
[22] M. Luysberg, R. G. S. Sofin, S. K. Arora, and I. V. Shvets, Phys. Rev. B **80**, 024111 (2009).
[23] A. Hamie, Y. Dumont, E. Popova, A. Fouchet, B. Warot-Fonrose, C. Gatel, E. Chikoidze, J. Scola, B. Berini, and N. Keller, Thin Solid Films **525**, 115 (2012).
[24] C. Kim, I. K. Robinson, J. Myoung, K. Shim, M. Yoo, and K. Kim, Appl. Phys. Lett. **69**, 2358 (1996).
[25] C. F. Chang, Z. Hu, S. Klein, X. H. Liu, R. Sutarto, A. Tanaka, J. C. Cezar, N. B. Brookes, H.-J. Lin, H. H. Hsieh, C. T. Chen, A. D. Rata, and L. H. Tjeng, Phys. Rev. X **6**, 041011 (2016).
[26] X. Liu, C.-F. Chang, D. Rata, Aurora, A. C. Komarek, and L. H. Tjeng, Npj Quantum Materials **1**, 16027 (2016).
[27] T. Yamanaka, N. Hirai, and Y. Komatsu, Am. Mineral. **87**, 1183 (2002).
[28] M. W. Haverkort, M. Zwierzycki, and O. K. Andersen, Phys. Rev. B **85**, 165113 (2012).
[29] Y. Lu, M. Höppner, O. Gunnarsson, and M. W. Haverkort, Phys. Rev. B **90**, 085102 (2014).
[30] M. W. Haverkort, G. Sangiovanni, P. Hansmann, A. Toschi, Y. Lu, and S. Macke, EPL **108**, 57004 (2014).
[31] F. de Groot and A. Kotani, *Core level spectroscopy of solids*, 1st ed. (CRC Press, 2008).
[32] T. Funk, A. Deb, S. J. George, H. Wang, and S. P. Cramer, Coord. Chem. Rev. **249**, 3 (2005).
[33] F. de Groot, Coord. Chem. Rev. **249**, 31 (2005).
[34] P. Carra, B. T. Thole, M. Altarelli, and X. Wang, Phys. Rev. Lett. **70**, 694 (1993).
[35] F. de Groot, Journal of Electron Spectroscopy and Related Phenomena **67**, 529 (1994).
[36] M. M. van Schooneveld, R. W. Gosselink, T. M. Eggenhuisen, M. Al Samarai, C. Monney, K. J. Zhou, T. Schmitt, and F. M. F. de Groot, Angew. **52**, 1170 (2013).
[37] P. Kuiper, B. Searle, L.-C. Duda, R. Wolf, and P. van der Zaag, J. Electron Spectros. Relat. Phenomena. **86**, 107 (1997).
[38] E. Goering, S. Gold, M. Lafkioti, and G. Schütz, Europhys. Lett. **73**, 97 (2006).
[39] E. Goering, M. Lafkioti, S. Gold, and G. Schütz, J. Magn. Magn. Mater. **310**, e249 (2007).
[40] C. Carvallo, P. Sainctavit, M. A. Arrio, N. Menguy, Y. Wang, G. Ona-Nguema, and S. Brice-Profeta, Am. Mineral. **93**, 880 (2008).
[41] H. Elnaggar, R.-P. Wang, S. Lafuerza, E. Paris, Y. Tseng, D. McNally, A. C. Komarek, H. Guo, M. Haverkort, T. Schmitt, and F. M. F. de Groot, ACS Appl. Mater. Interfaces **11**, 36213 (2019).
[42] R. A. D. Pattrick, G. van der Laan, C. M. B. Henderson, P. Kuiper, E. Dudzik, and D. J. Vaughan, Eur. J. Mineral. **14**, 1095 (2002).
[43] P. Kuiper, B. G. Searle, P. Rudolf, L. H. Tjeng, and C. T. Chen, Phys. Rev. Lett. **70**, 1549 (1993).
[44] D. Alders, L. H. Tjeng, F. C. Voogt, T. Hibma, G. A. Sawatzky, C. T. Chen, J. Vogel, M. Sacchi, and S. Iacobucci, Phys. Rev. B **57**, 11623 (1998).
[45] A. Scholl, J. Stöhr, J. Lüning, J. W. Seo, J. Fompeyrine, H. Siegwart, J.-P. Locquet, F. Nolting, S. Anders, E. E. Fullerton, M. R. Scheinfein, and H. A. Padmore, Science **287**, 1014 (2000).
[46] F. U. Hillebrecht, H. Ohldag, N. B. Weber, C. Bethke, U. Mick, M. Weiss, and J. Bahrdt, Phys. Rev. Lett. **86**,

3419 (2001).
[47] J. Lüning, F. Nolting, A. Scholl, H. Ohldag, J. W. Seo, J. Fompeyrine, J.-P. Locquet, and J. Stöhr, Phys. Rev. B **67**, 214433 (2003).
[48] M. W. Haverkort, S. I. Csiszar, Z. Hu, S. Altieri, A. Tanaka, H. H. Hsieh, H.-J. Lin, C. T. Chen, T. Hibma, and L. H. Tjeng, Phys. Rev. B **69**, 020408(R) (2004).
[49] E. Arenholz, G. van der Laan, R. V. Chopdekar, and Y. Suzuki, Phys. Rev. B **74**, 094407 (2006).
[50] M. Finazzi, A. Brambilla, P. Biagioni, J. Graf, G.-H. Gweon, A. Scholl, A. Lanzara, and L. Duò, Phys. Rev. Lett. **97**, 097202 (2006).
[51] C. Luo, H. Ryll, C. H. Back, and F. Radu (2018).
[52] G. van der Laan and B. T. Thole, Phys. Rev. B **43**, 13401 (1991).
[53] G. van der Laan, Phys. Rev. B **57**, 5250 (1998).
[54] S. S. Dhesi, G. van der Laan, E. Dudzik, and A. B. Shick, Phys. Rev. Lett. **87**, 067201 (2001).
[55] G. van der Laan, N. D. Telling, A. Potenza, S. S. Dhesi, and E. Arenholz, Phys. Rev. B **83**, 064409 (2011).
[56] S. Gota, M. Gautier-Soyer, and M. Sacchi, Phys. Rev. B **62**, 4187 (2000).
[57] C. T. Chen, Y. U. Idzerda, H.-J. Lin, N. V. Smith, G. Meigs, E. Chaban, G. H. Ho, E. Pellegrin, and F. Sette, Phys. Rev. Lett. **75**, 152 (1995).
[58] σ is also referred to as the fundamental spectra as in Refs.[61,62].
[59] M. W. Haverkort, N. Hollmann, I. P. Krug, and A. Tanaka, Phys. Rev. B **82**, 094403 (2010).
[60] H. Elnaggar, P. Sainctavit, A. Juhin, S. Lafuerza, F. Wilhelm, A. Rogalev, M.-A. Arrio, C. Brouder, M. van der Linden, Z. Kakol, M. Sikora, M. W. Haverkort, P. Glatzel, and F. M. F. de Groot, Phys. Rev. Lett. **123**, 207201 (2019).
[61] C. Brouder, J. Condens. Matter Phys. **2**, 701 (1990).
[62] C. Brouder, A. Juhin, A. Bordage, and M.-A. Arrio, J. Condens. Matter Phys **20**, 455205 (2008).